This is the accepted version of the following article:
Sazama, P., Kaucky, D., Moravkova, J., Pilar, R., Klein, P., Pastvova, J., . . . Mokrzycki, L. (2017). Superior activity of non-interacting close acidic protons in al-rich Pt/H-*BEA zeolite in isomerization of n-hexane. *Applied Catalysis A: General, 533*, 28-37. doi:10.1016/j.apcata.2016.12.016

This postprint version is available from URI: https://hdl.handle.net/10195/70260

Publisher's version is available from

https://www.sciencedirect.com/science/article/pii/S0926860X16306196?via%3Dihub

This postprint version is licenced under a Creative Commons Attribution-NonCommercial-NoDerivatives 4.0.International.

Superior activity of non-interacting close acidic protons in Al-rich Pt/H-*BEA zeolite in isomerization of *n*-hexane

Petr Sazama*, Dalibor Kaucky, Radim Pilar, Stepan Sklenak, Jaroslava Moravkova, Jana Pastvova, Barbara Supronowicz, Lukasz Mokrzycki, Petr Klein, Edyta Tabor

*J. Heyrovský Institute of Physical Chemistry, Academy of Sciences of the Czech Republic, Prague, Czech Republic, *E-mail: petr.sazama@jh-inst.cas.cz*

Abstract:

Skeletal isomerization of linear alkanes, an essential reaction for the production of gasoline, relies on environmentally questionable chlorinated catalysts, whose activity exceeds that of alternative zeolite catalysts. This work describes an attempt to understand relations between the local arrangement of active sites and skeletal isomerization of *n*-hexane in order to adapt the structure of zeolite catalysts to increase the reaction rates. For this purpose, we used a combination of synthesis of zeolites of *BEA structural topology with unique density and distribution of strongly acid sites, analysis of the nature of the acid sites by ^{1}H MAS NMR spectroscopy and FTIR spectroscopy of the OH groups and adsorbed d_3-acetonitrile, UV-VIS-NIR spectroscopy of carbocations formed by protonization, and kinetic analysis supplemented by DFT calculations of the reactant-active site interactions. We demonstrate that the high density of non-interacting but close and strongly acidic structural hydroxyl groups, which can enable the adsorption of reactant molecules mutually interacting in the confined reaction space, significantly lower the activation barrier in the isomerization reaction compared to far-distant acid sites. The Al-rich Pt/H-*BEA zeolite (Si/Al 4.2) with an unparalleled high concentration of the non-interacting close H^+ ions balancing the charge of the Al-Si-Al sequences forming a wall between the two channels yields 6 times higher reaction rates compared to state-of-the-art Si-rich Pt/H-zeolite catalysts.

Graphical abstract:

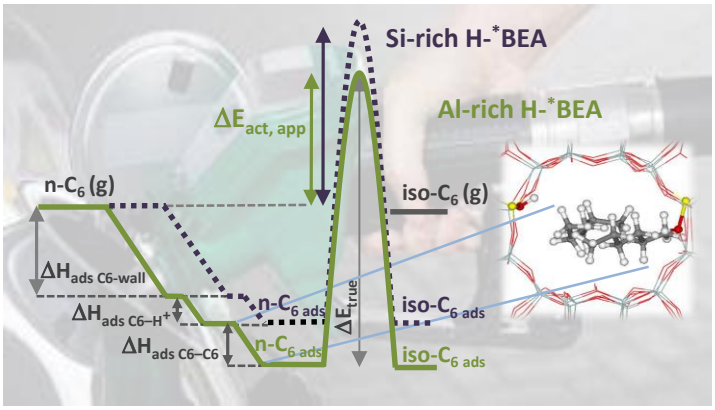

Keywords: Isomerization; Alkanes; Hexane; Zeolites; Al-rich beta (*BEA)

1. Introduction

Comprehending the consequences of the specific structure, arrangement and strength of Brønsted acid sites on skeletal isomerization of alkanes is important for the fundamental understanding of acid-catalyzed reactions over zeolite catalysts as well as for development of functional hydroisomerization catalysts. Hydroisomerization of linear alkanes into branched alkanes represents a key reaction for the production of automotive fuels. This complex catalytic reaction consists of dehydrogenation of a linear alkane to an alkene on a noble metal, skeletal isomerization of the formed alkene via protonization and a cyclopropyl intermediate on a strongly acidic site and re-hydrogenation of the branched alkene to the alkane (Figure 1).[1-4] The dehydrogenation/hydrogenation reactions on a bifunctional catalyst are in thermodynamic equilibrium and practically do not affect the reaction rate of the hydroisomerization.[4] In contrast, the acid-catalyzed reaction steps determine the rate of isomerization and require strongly acidic centers.[5] The labile protons of the O-H groups with acid strength strongly enhanced by the presence of chlorine on the traditional chlorinated Pt-alumina catalysts[6] provide sufficient conversion at temperatures as low as 150 °C.[7,8] Since the chlorination occurs by reversible chemical exchange of the surface hydroxyl groups of the alumina support, the use of this catalyst is associated with constant supply and formation of organic chlorines,[9] which leads to serious questions about the environmental impact. Zeolite-based acid catalysts, such as Pt-mordenite zeolite with improved texture[10-12] or sulfated Pt-zirconia[13,14] were developed; however, the acid centers of these catalysts facilitate a sufficient rate of isomerization at much higher temperatures. Conversely, low-temperature activity is crucial for achieving sufficient conversion of linear alkanes to branched ones due to the thermodynamic equilibrium of the isomerization reaction, wherein the lower temperatures shift the equilibrium towards the desired di-branched products, whereas higher temperatures hinder their formation. Development of an acidic catalyst for hydroisomerization of linear alkanes, particularly *n*-pentane and *n*-hexane, functional at low temperatures without streams containing low concentrations of chlorine additives, remains a great challenge for heterogeneous catalysis.

The fast dehydrogenation–hydrogenation reactions steps of the hydroisomerization process at Pt sites equilibrate alkanes and all alkene isomers of a given carbon chain structure providing a very low and constant concentration of alkenes that prevents their dimolecular reactions [5]. In the acid catalyzed reaction step, the transfer of acidic proton to the double bond of alkene molecule results in a transition state, the cyclopropyl carbonium ion, whose positive

charge is stabilized by an anion in the presence of superacids[15] or by covalent bonding to the framework oxygens in the zeolites[16] (Figure 1).

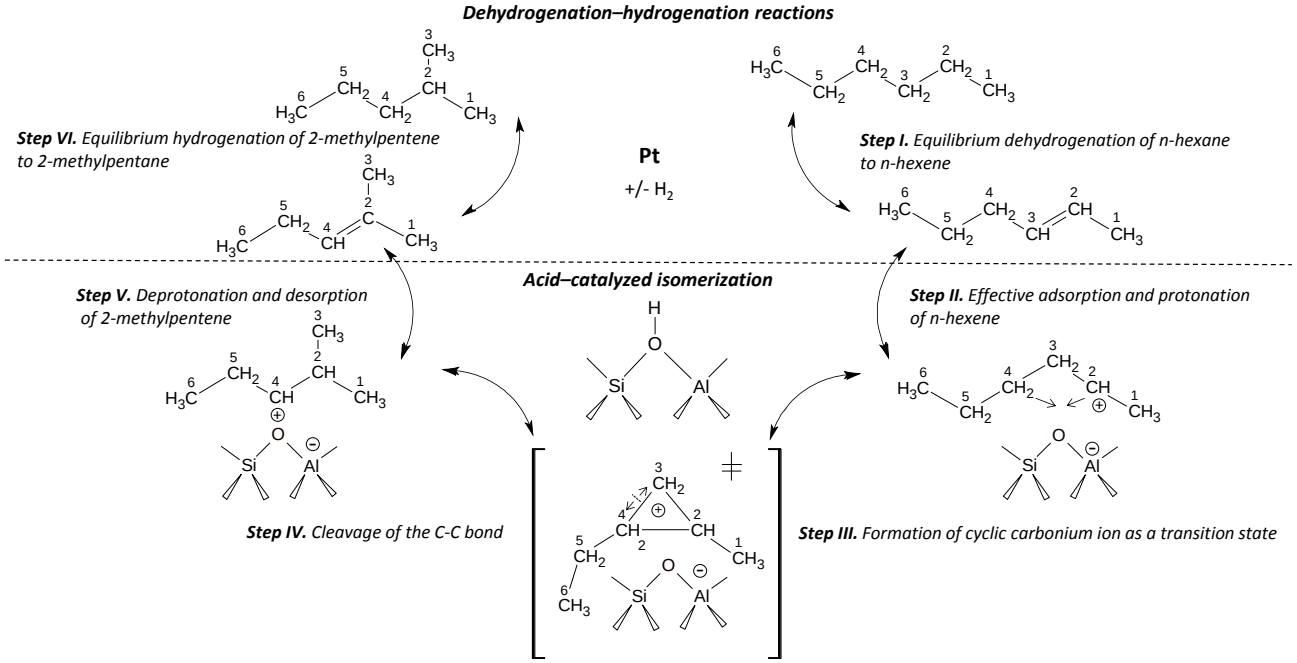

Figure 1. Illustration of the proposed complex reaction mechanism for *n*-hexane isomerization on bifunctional Pt/H-zeolite catalysts:
Step I. The fast dehydrogenation–hydrogenation at Pt sites equilibrates *n*-hexane and *n*-hexene providing a very low and constant concentration of *n*-hexene.
Step II. Effective adsorption and the transfer of acidic proton to the double bond of *n*-hexene (protonation) resulting in a 2-hexenium ion (linear secondary carbenium ion).
Step III. Formation of a transition state most likely in the form of 1-ethyl-2-methylcyclopropane carbocation (a cyclic carbonium ion) via bonding carbon atoms denoted as 2 and 4.
Step IV. Cleavage of the C-C bond between carbon atoms denoted as 3 and 4 of the cyclopropane carbocation resulting in the formation of 2-methyl-3-pentenium ion.
Step V. Deprotonation of 2-methyl-3-pentenium ion, formation of Brønsted OH group and desorption of 2-methylpentene.
Step VI. Equilibrium hydrogenation of 2-methylpentene to 2-methylpentane at Pt sites.

The charged transition state leads to a double bond and skeletal isomerization at low temperatures and, at high temperatures, ultimately also produces lower molecular weight alkanes, alkenes, and hydrogen[17]. Knaeble et al.[5] documented well that the rate of hexane skeletal isomerization at acid sites with an opened coordination sphere and located in an unconfined space in tungsten Keggin polyoxometalates supported on silica is proportional to the concentration of acid sites and decreases exponentially with decreasing acid strength. However, in the case of zeolite catalysts, the location of protons in the individual pores of high-silica zeolites and, in addition, the distances between the protons might be also expected to affect their function and reaction pathway in the isomerization reaction. The rate of skeletal isomerization per proton in the 8-member ring (8-MR) side channels of the mordenite

structure was reported to be five times higher in comparison with that in the large straight 12-member ring (12-MR) channels[18]. Since the pioneering work of Haag et al.[19], suggesting a linear relationship between the concentration of tetrahedral aluminum in the framework, hence the acid centers, and the reaction rate in the cracking of hexane, it has been well established that, not only the concentration, but also the local spatial arrangement of acidic centers attached to crystallographically different sites in the channels[20,21] and the distance between them[22] fundamentally influence both the reaction rate and the mechanism.

In pursuing the present work on understanding the isomerization of linear alkanes over zeolites, we wanted to specify the role of an increase in the density of the strongly acidic protons countering the negative charge of the framework in the H-forms of zeolites in relation to the occurrence of Al-Si-Al sequences, inevitably formed at high concentration of Al in the zeolite framework. We wanted to determine the effect of variations in the distribution of aluminum providing charge balance for the corresponding high concentration protons located in the close vicinity on the reaction rate and selectivity. We therefore employed zeolite *BEA topology, which can be prepared in a broad range of Al concentrations and which offers fast intra-crystalline diffusion of reactants and products through channels with three-dimensional architecture and 12-MR openings. We exploited recent progress in the synthesis of the beta zeolite that opened a new potential to manipulate the framework aluminum content in a very broad range and employed Al-rich beta zeolites with very high concentration of aluminum ($Si/Al \geq 4$) with highly predominant tetrahedrally coordinated Al in the framework[23-37]. This approach enabled us to examine the extent to which the isomerization reaction is affected by close proximity of strongly acidic centers. We found that the high density of non-interacting strongly acidic sites facilitates extraordinarily high reaction rates due to a synergetic effect significantly decreasing the activation barrier of the reaction. This enabled more rational design of isomerization zeolite catalysts providing superior activity.

2. Experimental

*2.1. *BEA and MOR zeolites and preparation of Pt/H-catalysts*

Al-rich beta zeolite (molar Si/Al 4.2), denoted as *BEA/4.2, was hydrothermally synthesized from aluminosilicate synthesis gel prepared from $NaAlO_2$ and fumed silica (Cabosil) in the absence of an organic structure-directing agent and using seeding of calcined beta crystals (TZB-212, Tricat). Details of the procedure were reported previously.[35] The high-silica zeolites used as standards for comparing the catalytic properties kindly supplied by the Tricat Company (now part of Clariant), (*BEA, Si/Al 11.5, TZB-212) and Zeolyst International

(*BEA, CP814B-25, Si/Al 12.5 and MOR, CBV 20A, Si/Al 12.1) were denoted as *BEA/11, *BEA/12, and MOR/12, respectively. A hierarchical mordenite zeolite with optimal micro-mesoporous structure was prepared and used for comparing the catalytic properties of Al-rich beta zeolite with a state-of-the-art hydroisomerization zeolite-based catalyst.[10] The hierarchical mordenite was prepared by treatment of MOR/12 in alkaline solutions (30 ml 0.2 M NaOH per 1 g mordenite stirred in a beaker at 85 °C for 2 h and subsequently in acid solution (10 ml 0.1 M oxalic acid per 1 g alkaline treated zeolite stirred in a beaker at 85 °C for 20 h). All the zeolites were ion-exchanged with 0.5 mol.dm^{-3} NH_4NO_3 at RT (1 g of a zeolite per 100 cm^3 of solution, three times over 12 h).

*BEA/4.2 consists of well-developed crystals ~ 0.4 μm in size with a surface area of 510 m.g^{-1} (Table 1). *BEA/11 and *BEA/12 consisted of very small crystallites ~ 0.05 and ~ 0.1 μm in size, respectively, and exhibited high surface areas of 617 and 605 m^2.g^{-1}, respectively. The intensities and patterns of the X-ray diffraction lines for the beta and mordenite zeolites are characteristic of the well-developed crystalline structure (Figure S1). The ^{29}Si MAS NMR spectra yielded framework Si/Al_{FR} ratio comparable with those obtained from the chemical analysis (Table 1).

Table 1. *Characteristics of the beta (*BEA) and mordenite zeolites.*

Sample	Zeolite	Si/Al[a]	Si/Al_{FR}[b]	c_{Al}[a] mmol.g^{-1}	c_B[c] mmol.g^{-1}	c_L[c] mmol.g^{-1}	Crystal size μm	S m^2.g^{-1}
H-*BEA/4.2	Al-rich *BEA	4.2	4.7	3.0	1.80	0.22	~0.4	510
H-*BEA/11	Si-rich *BEA	11.3	11.5	1.4	0.63	0.32	~0.1	617
H-*BEA/12	Si-rich *BEA	12.5	15.0	1.2	0.48	0.30	~0.1	605
H-MOR/12	Si-rich MOR	12.1	12.5	1.3	1.06	0.11	~0.3	454
H-MOR/10	Micro-mesoporous Si-rich MOR	9.5	11.2	1.6	0.77	0.35	~0.3	405[d]

[a] From chemical analysis of the Na^+ form of zeolites.

[b] From ^{29}Si MAS NMR spectra of the Na^+ form of zeolites.

[c] Concentration of Brønsted and Al-Lewis sites from FTIR spectra of adsorbed d_3-acetonitrile on the H^+ form of zeolites.

[d] External surface area 110 m^2.g^{-1}.

Pt was introduced into the zeolites by incipient wetness impregnation of pre-dried (105 °C/2 h) powder zeolites with a H_2PtCl_6 solution to yield 1.5 wt.% of Pt. The volume and

concentration of the solution was adjusted with respect to the porous volume of individual zeolite. The wet material was then dried overnight at 105 °C. The Pt-impregnated granulated zeolite was activated before the catalytic test in a stream of O_2 at 450 °C for 3 h, then purged by a N_2 stream at 450 °C, then cooled down to 250 °C, and finally activated in a mixture of 80 mol% H_2 and 20 mol% N_2 at 250 °C for 1 h.

2.2. Structural analysis

X-ray powder diffraction (XRD) patterns were obtained with a graphite monochromator and a position sensitive detector (Våntec-1) using a Bruker AXSD8 Advance diffractometer with CuKα radiation in Bragg–Brentano geometry. The porosity of the zeolites was determined by the analysis of the adsorption isotherms of nitrogen at 77 K carried out using an ASAP2010 apparatus (Micromeritics). Before the adsorption experiment the samples were outgassed at 240 °C for at least 24 hours. The crystal morphology was analyzed using a JEOL JSM-5500LV scanning electron microscope. The chemical compositions of the parent and prepared Pt-zeolites were determined by X-ray fluorescence spectroscopy using a PW 1404 (Philips). The FTIR spectra of the zeolites evacuated at 450, 500 and 550 °C were recorded at RT on a Nicolet Nexus 670 FTIR spectrometer equipped with a MCT-B detector operating at 1 cm^{-1} resolution by collecting 256 scans for a single spectrum. The concentration of acidic Brønsted and Lewis sites in H-zeolites was determined by the adsorption of d_3-acetonitrile (13 mbar CD_3CN at RT for 20 min with a subsequent evacuation for 15 min at RT) from the intensities of the characteristic IR bands of the C≡N vibrations according to the procedure described by Wichterlova et al. [38]. The extinction coefficients used for the corresponding C≡N vibrations were ε_B = 2.05 cm.μmol^{-1} and ε_L = 3.60 cm.μmol^{-1}.[38] Solid state ^{1}H and ^{29}Si MAS NMR experiments were carried out on a Bruker Avance 500 MHz Wide-Bore spectrometer (11.7 T) equipped with 4 mm double-resonance MAS NMR probe-head. ^{1}H MAS NMR single pulse spectra were collected after 128 scans with a $\pi/2$ (4 μs) excitation pulse and 2s repetition delay at a rotation speed of 11 kHz. To obtain the protonic form (H-*BEA), "parent" NH_4-*BEA samples were dehydrated *in-situ* in 4 mm ZrO_2 MAS NMR rotors at 450 °C (ramp 1 °C.min^{-1}) under dynamic vacuum of 5.10^{-1} Pa for 6 hours. ^{29}Si MAS NMR single pulse spectra of hydrated zeolites were measured at a rotation speed of 7 kHz, with a π/6 (1.7 μs) excitation pulse and relaxation delay of 30 s for single pulse spectra. The framework aluminum content (Si/Al_{FR}) was estimated from the intensity of the ^{29}Si NMR resonances according the equation $Si/Al_{FR} = I/(0.25\ I_1 + 0.5\ I_2)$, where I, I_1, and I_2 correspond to the total, Si(3Si,1Al), and Si(2Si,2Al) intensity.[39,40] The UV–Vis spectra of Al-rich and Si-rich H-

*BEA zeolites dehydrated at 500 °C in a vacuum after interaction with hexamethylbenzene (HMB) at 200 °C for 1, 2 and 3 h and after subsequent interaction with NH_3 were measured in the range from 20 000 to 45 000 cm^{-1} using a Perkin-Elmer Lambda 950 spectrometer equipped with a Spectralon integration sphere. HMB was introduced into the dehydrated zeolite by mixing the powdered zeolite and HMB in a glovebox and the measurements were performed using a cell enabling collection of the spectra without exposure of the mixture to the air.

2.3. Kinetic analysis

The kinetic analysis of hydroisomerization of *n*-hexane to the corresponding *iso*-hexanes was performed in a regime implying equilibrium between hydrocarbons in the micropores and gas phase reached by a high H_2/hydrocarbon molar ratio and correspondingly low concentration of hexanes in the reaction stream.[41] The kinetic regime under the reaction conditions was confirmed by variation in the total gas flow and the weight of the catalyst. Small crystallites of the zeolites (~ 0.05 – 0.4 μm) guaranteed the absence of intra-crystalline diffusion constraints to the overall reaction rates. The concentration of platinum of 1.5 wt.% in the prepared PtH-zeolite catalysts provides a sufficient rate of (de)hydrogenation reactions yielding hexene/hexane in equilibrium and not limiting the overall alkane hydroisomerization.[41] The catalytic tests were carried out in a glass flow-through tubular U-shaped reactor under atmospheric pressure. 0.50 g of a catalyst and the reaction stream consisting of 79 mol% H_2, 20 mol% N_2 and 1 mol% of hexane kept at a total flow rate 66 $cm^3.min^{-1}$ corresponded to WSHV 0.25 h^{-1} and GHSV 4000 h^{-1}. The temperature of the reactor was controlled with an internal thermocouple and kept at the desired temperature in the range 125 – 250 °C. The concentrations of *n*-hexane, branched hexanes and lower molecular weight products (methane, ethane, propane, butane, and *iso*-butane) were analyzed by an on-line connected Finnigan 9001 gas chromatograph equipped with a 50m×0.32mm×5μm Al_2O_3/KCl capillary column and an FID detector. Steady-state conditions were achieved within 0.5 - 3 h of reaction time-on-stream. The reaction rates of the *n*-hexane to *iso*-hexane were calculated at low conversion values and close to 100% selectivity for *iso*-hexanes. Only the conversion values <6% are considered for our calculation of the reaction rates ($mol_{iso\text{-}hexanes}.g_{cat}^{-1}.s^{-1}$) and the TOF values for the reaction per Al ($mol_{iso\text{-}hexanes}.mol_{Al}^{-1}.s^{-1}$).

The conversions and yields of branched hexane isomers and lower molecular weight by-products were also analyzed under process-like conditions. These catalytic tests were

performed using a stainless-steel gas flow tubular PID Eng&Tech Microactivity – Reference reactor at a pressure of 10 bar with a H_2 to hexane molar ratio of 6 and amount of catalyst equal to 2.5 g (5 ml) with a flow rate corresponding to WHSV 0.7 h^{-1} and GHSV 638 h^{-1}. The temperature was controlled by an internal thermocouple and kept at the desired temperature in the range 200 - 215 °C. Liquid *n*-hexane was continuously loaded by a Gilson 307 pressure pump and evaporated in the hot flow of hydrogen gas. The reaction products were analyzed using an on-line connected Perkin Elmer Clarus 580 gas chromatograph equipped with CP-Sil Pona CB column (100 m x 0.25 mm x 0.5 μm) and an FID detector.

2.4. Periodic DFT Molecular Dynamics calculations

Computational models. Three models of the beta zeolite with P1 symmetry featuring 1, 3, and twenty-seven *n*-hexane molecules in a super cell composed of four *BEA unit cells, denoted as $Model_{ISOL}$, $Model_{DIMER}$, and $Model_{TRIMER}$, respectively, were used to study the adsorption of *n*-hexane on acidic Brønsted sites of the beta zeolite. $Model_{ISOL}$ was used to study the adsorption of mutually non-interacting *n*-hexane molecules on distant acidic Brønsted sites. $Model_{DIMER}$ was employed to investigate the formation of the hexane – hexane dimer on two close acidic Brønsted sites while $Model_{TRIMER}$ was used to study the creation of a hexane – hexane – hexane trimer on three close acidic Brønsted sites. The three and twenty seven *n*-hexane molecules in the zeolite were used only for the molecular dynamics simulations while the geometry optimizations were carried out with two and three hexane molecules, forming a dimer and trimer, respectively.

A super cell composed of four unit cells, two along the *a* dimension and two along the *b* dimension, was employed (cell parameters, a = 25.264, b = 25.264, c = 26.186 Å) for all three models. Each of the four unit cells was the same as that used in model 5, variant 1, of our prior investigation,[35] i.e., the Al distribution was identical. All the AlO_4^- tetrahedra were compensated for by protons in the AlOHSi groups.

Electronic structure calculations. Periodic DFT calculations were carried out employing the VASP code.[42-45] The Kohn-Sham equations were solved variationally in a plane–wave basis set using the projector-augmented wave (PAW) method of Blöchl,[46] as adapted by Kresse and Joubert.[47] The exchange-correlation energy was determined using the Perdew-Burke-Ernzerhof (PBE) functional.[48] Brillouin zone sampling was restricted to the Γ-point. A plane-wave cutoff of 400 eV (PREC = Accurate) was employed for the geometry optimizations, while a smaller cutoff of 300 eV was used for the molecular dynamics simulations. The dispersion energy is calculated employing the method of Tkatchenko and Scheffler[49,50] for the

geometry optimizations while the D2 method of Grimme[51] is utilized for the molecular dynamics simulations.

Geometry optimizations. The atomic positions were optimized by employing a conjugate-gradient algorithm minimization of energies and forces while the lattice parameters were fixed (constant volume) at their experimental values.

Molecular dynamics. The molecular dynamics (MD) simulations used the exact Hellmann-Feynman forces acting on atoms and applied the statistics of the canonical ensemble to the motion of the atomic nuclei using the Verlet velocity algorithm to integrate Newton's equations of motion. The time step for the integration of the equations of motion was 1 fs. The simulation was run for 10000 fs at 300 K for all three computational models. The structures of 17 distinct ″snapshots″ collected each 500 fs from step 2000 to step 10000 of the molecular dynamics simulations were optimized and used to estimate the adsorption energy employing the average value from the seventeen ″snapshots″.

Adsorption energies. The adsorption energy ΔE_{ads1} of isolated (i.e., mutually non-interacting) *n*-hexane molecules on the beta zeolite was calculated as the difference between the energy of $Model_{ISOL}$ (beta zeolite + one *n*-hexane) and the sum of the energies of the empty beta zeolite and isolated n-hexane calculated in the empty unit cell with the same cell parameters as $Model_{ISOL}$. The adsorption energies ΔE_{ads2} of the *n*-hexane – *n*-hexane dimer and ΔE_{ads3} of the *n*-hexane – *n*-hexane – *n*-hexane trimer were calculated in the same manner as ΔE_{ads1}. The energy of $Model_{DIMER}$ (beta zeolite + two *n*-hexane molecules) and $Model_{TRIMER}$ (beta zeolite + three *n*-hexane molecules) was used instead of that of $Model_{ISOL}$, and the energies of two and three isolated *n*-hexane molecules instead of that of single isolated *n*-hexane. The calculated values of ΔE_{ads2} and ΔE_{ads3} were divided by 2 and 3, respectively, to obtain the adsorption energy per adsorbate molecule.

3. Results and discussions

3.1. Analysis of acid sites

The pair of samples H-BEA/4.2 and H-BEA/11 zeolites, exhibiting different concentration of the framework Al atoms corresponding to molar Si/Al_{FR} 4.7 and 11.5, respectively (Table 1), was analyzed for the concentration and strength of the Brønsted sites, the concentration of Lewis acid sites and the presence of structural defects using ^{1}H MAS NMR spectroscopy, FTIR spectroscopy of the OH groups and adsorbed d_3-acetonitrile, and UV-VIS-NIR spectroscopy of carbocations formed by protonization upon adsorption of hexamethylbenzene (HMB). The ^{1}H MAS NMR spectra of the dehydrated H-*BEA/4.2 and H-*BEA/11 zeolites

(Figure 2A) exhibit bands with maxima at 1.6, 2.0, 2.4-2.5, and 3.6-3.8 ppm characteristic of terminal and internal SiOH, extra-framework AlOH and bridging Si(OH)Al groups, respectively.[52,53] The main difference in the spectra of H-*BEA/4.2 and H-*BEA/11 is in the intensity of the signal characteristic of bridging Si(OH)Al groups. The 3 times higher intensity of the signal of the Brønsted sites for H-*BEA/4.2 corresponds to the increase in the concentration of Al in the zeolite with Al atoms incorporated predominantly in the regular T_d coordination in the framework. The close positions of the band maxima at 3.6 and 3.8 ppm for Si- and Al-rich *BEA, respectively, can indicate that the acid strength does not greatly differ. The maxima of the signals of the OH groups in the zeolites are not unambiguously connected with their acid strengths; however, the shift matches the changes in properties for a single zeolitic structure.[54,55] The signal of silanol groups forming a surface termination of the crystalline structure is weak for H-*BEA/4.2 due to the low external surface of well-developed crystallites compared to high intensity of the band for *BEA-11 characteristic of small crystallites. It is obvious that the signal of the internal silanol groups reflecting structural defects associated with removal of the T-atoms or intergrowth structure also exhibits barely distinguishable intensity for the Al-rich *BEA sample compared to the Si-rich *BEA. As the intensities of the ^{1}H MAS NMR bands do not depend on the band positions, they accurately reflect the ratio between the concentrations of the individual hydroxyls. Thus the low intensity signal of the internal silanol groups and the low signal of the OH groups bound to extra-framework and/or perturbed framework Al atoms indicate that the Al-rich *BEA/4.2 sample has a well-developed low-defective crystalline structure.

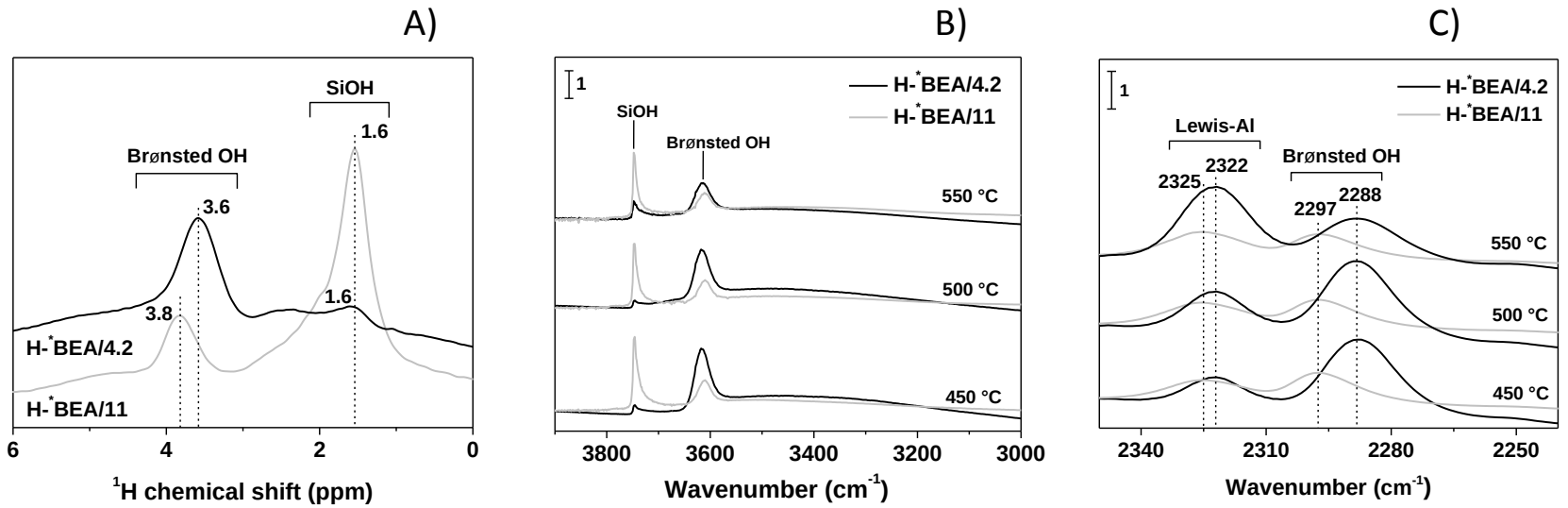

Figure 2. Analysis of acid sites in H-*BEA zeolites. A) ^{1}H MAS NMR spectra of H-*BEA zeolites dehydrated at 500 °C, and FTIR spectra for zeolites dehydrated at increasing temperatures in B) the region of the $\nu_{0\rightarrow1}$OH vibration and C) in the region of the $\nu_{0\rightarrow1}$C≡N vibration after adsorption of d_3-acetonitrile.

Figures 2B and 2C show the FTIR spectra in the region of hydroxyl group vibrations of H-*BEA/4.2 and H-*BEA/11 evacuated at temperatures from 450 up to 550 °C and after adsorption of d_3-acetonitrile, respectively. The FTIR spectra in the region of the hydroxyl group exhibit approximately 3 times higher intensity of the bands with maxima at about 3610 - 3613 cm^{-1} of the stretching vibration of the bridging hydroxyls, negligible intensity of the bands at 3650 - 3660 cm^{-1} of perturbed framework or extra-framework AlOH[56-58] and low intensity of the band at 3727 - 3745 cm^{-1} of silanols for the H-*BEA/4.2 sample compared to H-*BEA/11 in good agreement with the ^{1}H MAS NMR results. Only evacuation at 550 °C produced a considerable loss of the intensity for the bridging hydroxyls. This indicates sufficient structural stability of Al-rich H-*BEA zeolite at temperatures relevant for the isomerization reactions. Adsorption of d_3-acetonitrile resulted in the appearance of the bands at 2325 and 2297 cm^{-1} corresponding to the stretching mode of ν(C≡N) of d_3-acetonitrile adsorbed on Lewis and Brønsted sites, respectively.[38] Quantitative analysis of the acid sites using the integral intensities of the IR bands and the extinction coefficients for the C≡N group interacting with the Brønsted and Lewis sites[38] indicated a slightly predominant concentration of Brønsted sites compared to concentration of Lewis sites in the H-*BEA/4.2 sample (table 1). The formation of a significant concentration of Lewis sites is connected with a reversible change in the coordination of the framework Al atoms characteristic of the structure of the *BEA zeolite[36,59-64] and also observed for Al-rich *BEA.[65] Thus the ^{1}H MAS NMR and FTIR spectra and OH groups and adsorbed d_3-acetonitrile together show that the increase in the concentration of the aluminum content does not led to significantly increased dehydroxylation and formation of Lewis acid sites and the concentration of Brønsted hydroxyls in Al-rich beta zeolite is proportional to the increase in the concentration of Al in the zeolite framework.

The ability of the Brønsted hydroxyls to protonate hexene, the essential step in the isomerization reaction (Step II in Figure 1), is controlled by interplay of the concentration and strength of the acidic centers and confinement of the hydrocarbon molecule in a constrained environment of the zeolite channels.[18] However, the protonation of hexene cannot be experimentally followed because of the unmeasurable hexene concentration under realistic reaction conditions and at higher concentrations due to the rapid oligomerization of the akenes and the formation of complex hydrocarbon molecules.[66] Therefore, the ability of Al-rich H-*BEA zeolite to form carbenium ions was analyzed using the hexamethylbenzene (HMB) molecule, whose protonation yields the relatively stable hexamethylbenzenium cation providing electronic transitions with characteristic spectral components in the range of UV-Vis light.[67] The UV-Vis spectra of HMB and carbocations formed by protonization of

adsorbed hexamethylbenzene (HMB) in Al-rich and Si-rich H-*BEA zeolites are shown in figure 3. The UV-Vis spectrum of neutral HMB exhibited a typical absorption band at 37 000 cm^{-1} characteristic of the π-electron system of the aromatic ring.[68] Adsorption of HMB in both Si- and Al-rich *BEA zeolites resulted in the appearance of an intense band with maximum at 25 500 cm^{-1} with a shoulder around 29 500 cm^{-1} corresponding to the formation of the hexamethylbenzenium cation.[67,69] The spectra obtained for the two zeolites do not show significant differences in the positions and shapes of the high intensity bands of the carbenium ions and are very similar to those of protonated benzene in a superacidic solution.[68] The assignment of the bands to the hexamethylbenzenium cation was demonstrated experimentally by co-adsorption of ammonia, resulting in disappearance of the band at 25 500 cm^{-1} consistent with proton transfer between ammonia as a stronger base and the hexamethylbenzenium cation forming the ammonium ion and neutral HMB.

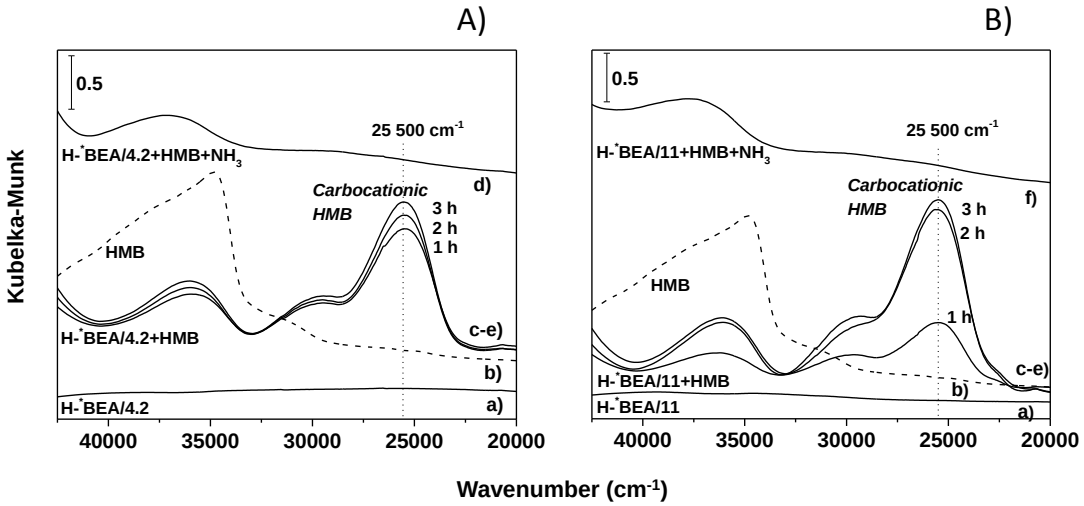

Figure 3. UV-vis spectra of carbocations formed by protonization of hexamethylbenzene (HMB) in A) Al-rich and B) Si-rich H-*BEA zeolites. Spectra of a) zeolites dehydrated at 500 °C, b) solid HMB, c-e) zeolite after interaction with HMB at 150 °C for 1, 2 and 3 h, respectively, and d) after subsequent interaction with NH_3.

*3.2. Nature and local arrangement of acid sites in Al-rich H-*BEA*

The negligible intensity of the internal silanol groups, the low signal of the OH groups bound to extra-framework and/or perturbed framework Al atoms and very high intensity of the structural bridging OH groups observed in the ^{1}H MAS NMR and FTIR spectra of Al-rich H-*BEA are consistent with non-defective crystalline structure with a high concentration of non-interacting (isolated) acid sites associated with tetrahedrally coordinated Al atoms in the

zeolite framework. In Al-rich *BEA zeolites (Si/Al 4–5), the Al atoms are predominantly present in the Al-Si-Al sequences[30,35,65,70] with the concentrations of Al-Si-Al ranging from 40% to 100% of the total Al depending on their arrangement in rings or as long sequences.[65] It follows that the majority of the H^+ ions in the H-*BEA/4.2 sample compensate the negative charge resulting from substitution of the framework Si(IV) by Al(III) in the Al-Si-Al sequences; however, the respective OH groups are reflected in the ^{1}H MAS NMR and FTIR spectra as non-interacting OH groups. Our previous ^{27}Al and ^{29}Si (CP) MAS NMR studies supplemented by FTIR of adsorbed d_3-acetonitrile and UV–Vis spectroscopy of Co(II) ions as probes of close Al atoms and further supported by DFT molecular dynamic calculations of the Co(II) sites in the *BEA zeolites revealed that these Al-Si-Al sequences in Al-rich *BEA zeolites are mostly located in the zeolite wall separating two channels and the Al atoms of the sequence thus face two channels (see Figure 4 and Ref. [65]). The negative charge of the framework originating from these sequences is balanced by two H^+ ions located in different channels. Therefore the high concentration of Al atoms in the framework of Al-rich beta zeolites does not result in increased formation of interacting OH groups but the Al-Si-Al sequences forming the zeolite beta wall provide H^+ sites like in a Si-rich zeolite but in significantly increased concentrations. The calculated deprotonation energies used as a measure of the acid strengths of the Brønsted sites corresponding to AlSiAl and AlSiSiAl sequences in Al- and Si-rich *BEA, respectively, reported in the previous study,[35] were in the range of differences in the deprotonation energy values among the protons associated with AlOHSi groups at individual T sites in the framework of *BEA zeolites. This is consistent with the small observed shift in the maxima of the band of bridging hydroxyl groups in the ^{1}H MAS NMR and FTIR spectra, and the similar protonating ability of HMB molecules. The pair of Al- and Si-rich H-*BEA zeolites thus represents unique material that allows elucidation of the effect of the close vicinity of non-interacting acidic protons on activation of a hydrocarbon molecule in acid-catalyzed reactions over zeolite catalysts, moreover, in the three-dimensional channel system with 12-MR openings providing easy intra-crystalline diffusion of reactants and products.

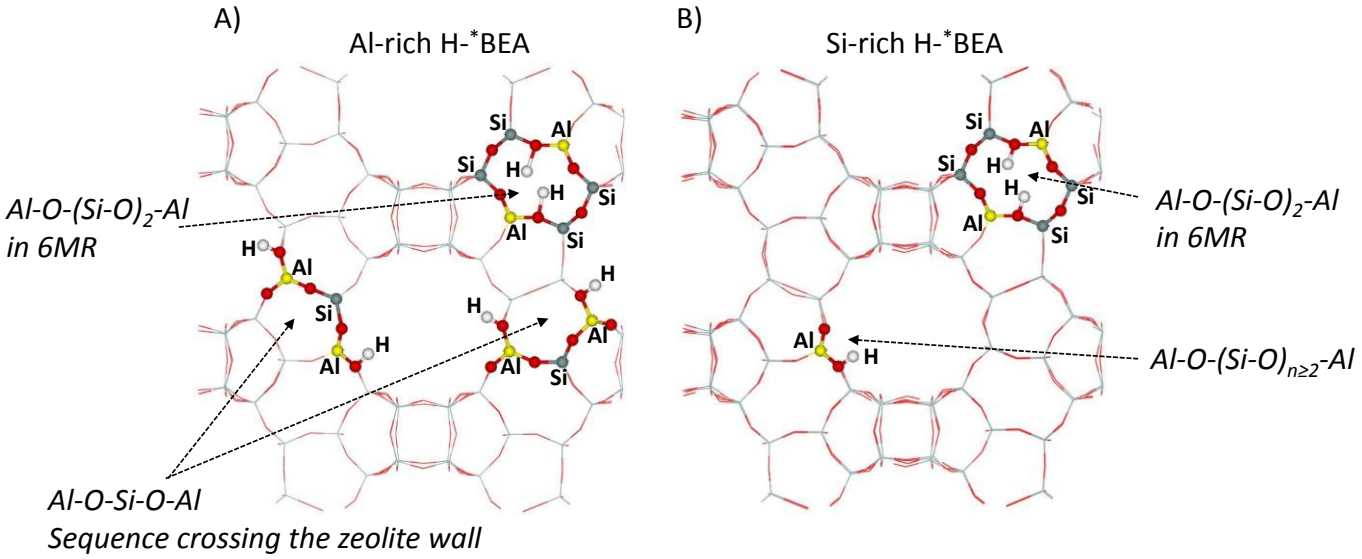

Figure 4. Schematic representations of the main Al-O-$(SiO)_n$-Al sequences in A) Al-rich and B) Si-rich H-*BEA zeolites. H^+ compensates the charge mainly from Al-O-Si-O-Al sequences in Al-rich H-*BEA whereas the closest Al atoms form an Al-O-$(SiO)_2$-Al sequence in Si-rich H-*BEA. The Al-O-Si-O-Al sequences cross the zeolite wall and the corresponding H^+ are located in two different channels in Al-rich H-*BEA. Oxygens in red.

3.3. The effect of the density of acid sites on n-hexane isomerization

Figure 5 depicts the yields of branched hexanes and low molecular products as a function of temperature and Arrhenius plots for hydroisomerization of *n*-hexane over Al- and Si-rich Pt/H-*BEA zeolites. The high concentration of close strongly acidic sites in Al-rich *BEA led to a greatly improved yield of branched isomers with very low yield of undesired C_1-C_4 products compared Si-rich *BEA zeolites over the entire temperature range from 150 to 225 °C. The high density of Brønsted sites facilitated dramatically increased conversion of *n*-hexane to *iso*-hexane from 5.9 to 35.5% practically without formation of side-products (0.2% yield of C_1-C_4) at 175 °C (table S1). The reaction rate per gram of Al-rich *BEA zeolite exceeds six fold that of Si-rich *BEA (table 2). More than twice higher TOF calculated per total concentration of Al for Al-rich *BEA clearly shows the substantially higher specific activity of the active sites. The remarkable improvement in the catalytic performance is reflected in the lower apparent activation energy of 104.2 vs. 118.9 kJ.mol^{-1} obtained from the Arrhenius plots for Al- and Si-rich *BEA, respectively, in accordance with the higher specific activity of the active sites. The six-fold higher reaction rate, higher TOF and the lower apparent activation energy by ca. 15 kJ.mol^{-1} for Al-rich *BEA zeolite clearly indicate a synergistic effect of the high concentration and close proximity of the OH groups.

Table 2. Hydroisomerization of *n*-hexane to 2-methyl- and 3-methylpentanes, reaction rates (r_{ISO}) and turnover frequencies (TOF) for 145 °C.

Sample	[a] y_{iso-C6} %	r_{iso} mol.g^{-1}.s^{-1}	[b] TOF s^{-1}.10^4
PtH-BEA/4.2	5.68	5.7 10^{-8}	1.8 10^{-5}
PtH-BEA/12	0.99	9.8 10^{-9}	8.1 10^{-6}

Reaction conditions: WHSV 0.25 h^{-1}, molar ratio H_2/n-C_6 79, atmospheric pressure.

[a] yield of 2-methyl- and 3-methylpentanes while the formation of di-branched hexane isomers and lower molecular weight by-products was negligible

[b] TOF calculated for total concentration of Al

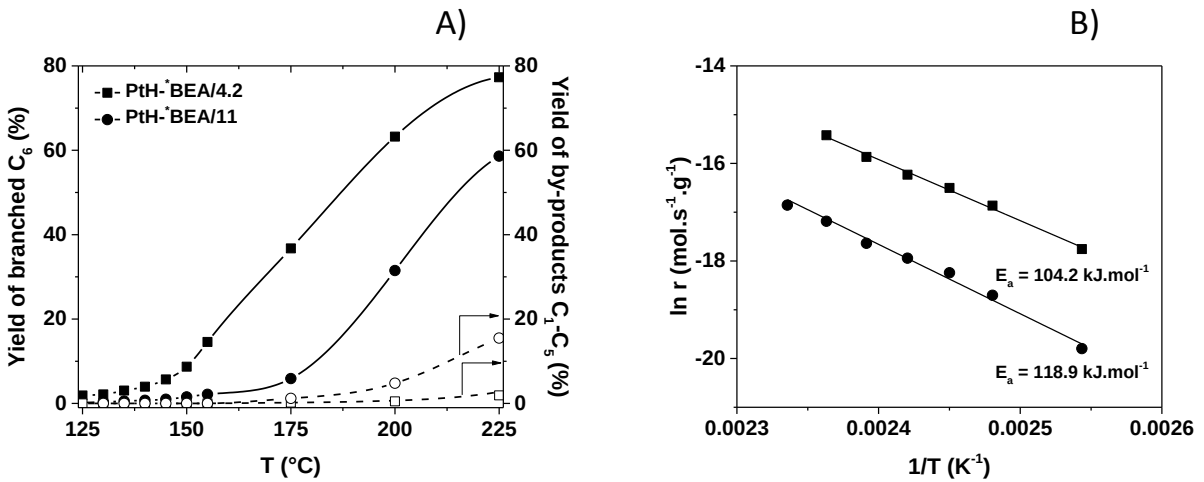

Figure 5. Hydroisomerization of *n*-hexane over Al-rich *BEA (PtH-*BEA/4.2) compared with Si-rich *BEA zeolite (PtH-*BEA/11). A) Effect of temperature on the yields of branched C_6 isomers and C_1-C_5 by-products, and B) Arrhenius plot and the apparent activation energy calculated considering the low conversion values.

3.4. The enhancement of the reaction rate over proximate non-interacting OH groups

The reduced apparent activation energy and increased TOF for Al-rich H-*BEA zeolite indicate only a partial contribution of the increased concentration of protonic sites to the overall enhancement of the catalytic properties and therefore another factor associated with the close proximity of the active sites plays an important role. The apparent activation energy for the acid catalyzed steps of the isomerization over H-zeolites can be expressed in the absence of diffusion limitations as the difference between intrinsic activation energy $\Delta E_{act,true}$ and the adsorption energy ΔE_{ads} according Eq. 1

$$\Delta E_{act,\,app} = \Delta E_{act,true} - \Delta E_{ads} \qquad \text{Eq. (1).}$$

In general, the apparent activation energies decrease monotonously and the reaction rates increase exponentially with the carbon number in the molecule of linear hydrocarbons for acid-zeolite-catalyzed reactions.[71,72] Accurate measurements of the reaction rates for alkane cracking and adsorption thermodynamics explained the observed dependences on the number of carbon atoms by the contribution of the adsorption energy increasing monotonously with carbon number for *n*-alkanes. Correcting the apparent activation energy by the heat of adsorption (Eq. 1) has led to the generally accepted conclusion that the intrinsic activation energies are similar for all C_3-C_{20} hydrocarbons.[71-75] Computation studies in agreement with the rigorous experimental measurements documented that the intrinsic activation barrier for C_3-C_{20} alkanes on H-zeolites equals approximately 180 - 190 kJ.mol^{-1}.[71,72]. E.g., the apparent activation energy for monomolecular cracking of hexane and propane over ZSM-5 zeolites decreases from approximately 145 kJ.mol^{-1} to 110 kJ.mol^{-1} and the adsorption energy increases from 40 kJ.mol^{-1} to 75 kJ.mol^{-1} providing similar intrinsic activation energies of ~ 185 kJ.mol^{-1}.[72] It is obvious that the interaction of a hydrocarbon molecule in the confined reaction space with inner walls of the zeolite channels is an important factor controlling the apparent activation energy of acid catalyzed reactions and the corresponding reaction rate in zeolites, while the presence of strongly acidic active sites is a necessary condition for occurrence of the reaction.

The proximity of the non-interacting Brønsted hydroxyl groups in Al-rich H-*BEA could enable a mutual interaction of hydrocarbon molecules upon adsorption on the adjacent active centers that could affect the catalytic reaction compared to mutually distant active centers. We studied whether the proximity of the active centers can lead to a mutual interaction of C_6 hydrocarbon molecules in a model Al-rich H-*BEA using DFT calculations. The saturated alkane (*n*-hexane) rather than the corresponding unsaturated alkene (*n*-hexene) was chosen to computationally investigate the adsorption of hydrocarbons. The former is

significantly less reactive than the latter while the contribution of the mutual interactions to the overall adsorption energies should be comparable. The mutual interaction of hydrocarbon is given by the dispersion energy – non-bonding interactions of the atoms of the hydrocarbon. The difference between *n*-hexane and *n*-hexene is only one single C-C versus double C=C bond, respectively, and two more hydrogen atoms of *n*-hexane. The available experimental energies for a mutual interaction of alkanes in zeolites in the literature[76] enable comparison for the calculated and measured values. The heats of adsorption for alkenes could not be measured because of their reaction on acidic OH groups[77] and a rigorous computation approach is highly complicated by the complex interaction of the molecule with double bond with zeolite. The analysis of energy contributions due to mutual interactions of C_6 molecules employing only *n*-hexane molecules in the computational models cannot provide rigorous assessment, but the approximation provides a relevant estimation of an increase in the adsorption energy if the reactant molecules mutually interact on close active sites. The interaction of the *n*-hexane molecule with the acid sites (host−guest), lateral interaction with the zeolite lattice (host−guest) and direct interaction between the *n*-hexane molecules (guest–guest; i.e., dimer and trimer) were analyzed by modeling the Al-rich H-*BEA zeolite using periodic DFT Molecular Dynamics (MD) calculations with subsequent optimizations. The adsorption energy ΔE_{ads1} of isolated (i.e., mutually non-interacting) *n*-hexane molecules on the beta zeolite was calculated as the difference between the energy of $Model_{ISOL}$ (beta zeolite + one *n*-hexane) and the sum of the energies of the empty beta zeolite and isolated *n*-hexane calculated in the empty unit cell with the same cell parameters as $Model_{ISOL}$. The adsorption energies ΔE_{ads2} of the *n*-hexane – *n*-hexane dimer and ΔE_{ads3} of the *n*-hexane – *n*-hexane – *n*-hexane trimer were calculated in the same manner as ΔE_{ads1}. The energy of $Model_{DIMER}$ (beta zeolite + two *n*-hexane molecules) and $Model_{TRIMER}$ (beta zeolite + three *n*-hexane molecules) was used instead of that of $Model_{ISOL}$, and the energies of two and three isolated *n*-hexane molecules instead of that of single isolated *n*-hexane. Our DFT calculations yielded a calculated adsorption energy greater by 11 and 12 $kJ.mol^{-1}$, when the *n*-hexane dimer (Figure 6) and trimer were formed, respectively, compared to isolated mutually non-interacting *n*-hexane molecules. Twenty seven *n*-hexane molecules (in the super cell composed of four *BEA unit cells) had to be used for our molecular dynamics simulations to obtain one trimer, indicating that trimers are formed only at a higher loading of *n*-hexane in the zeolite. The tiny difference between the ΔE_{ads2} and ΔE_{ads3} values and the fact that trimers are formed only at higher loadings indicate that mainly the formation of dimers can be responsible for the increase in the adsorption energy. This result is in agreement with the experimental results on

H-FAU, showing that the adsorbed molecules can interact with at most two other adsorbed molecules.[76] Our theoretical results showed that the intermolecular interactions could be of high importance for the Al-rich H-*BEA zeolite. The DFT results are consistent with the experimental study of Eder and Lercher,[76] showing that the adsorption heat increases by a maximum of ~ 20 $kJ.mol^{-1}$ due to mutual interactions of the *n*-hexane molecules in the 12-MR zeolite hosts.

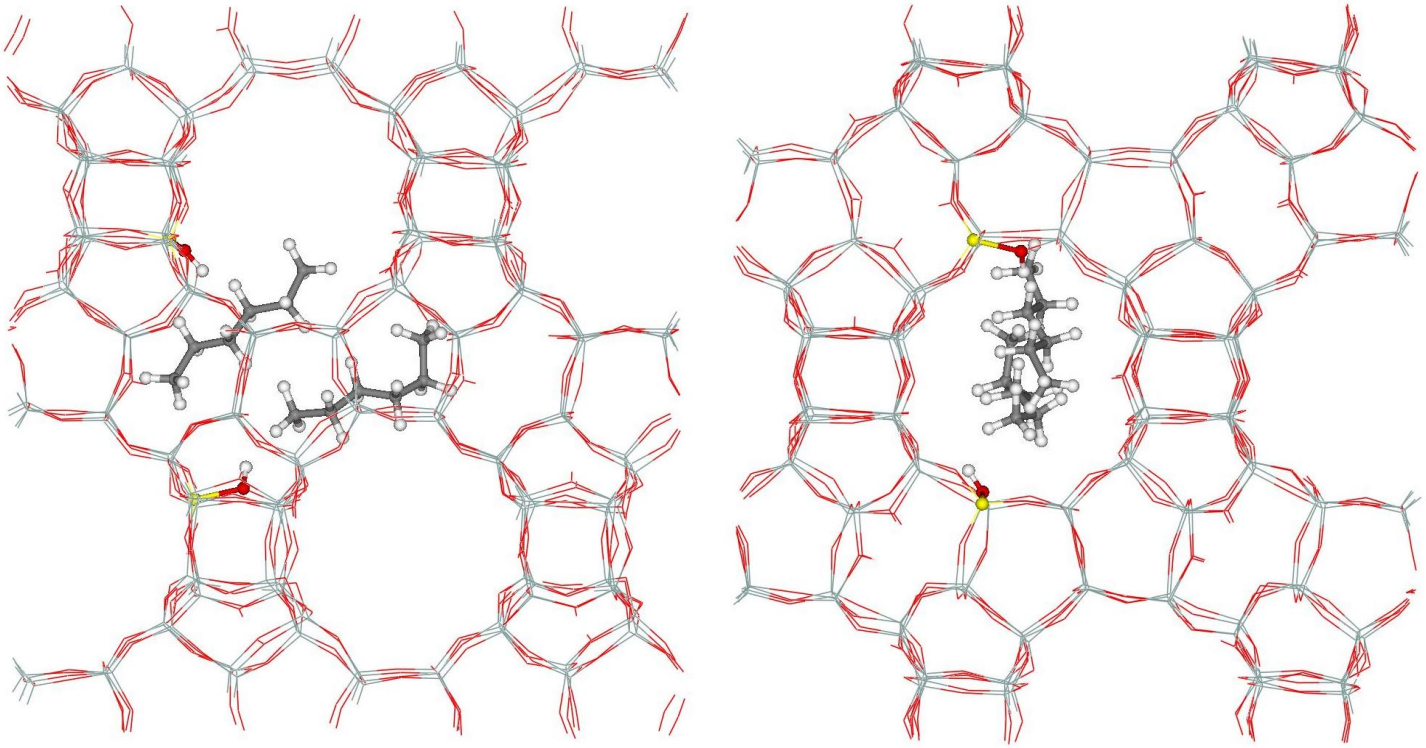

Figure 6. Optimized structure of the adduct with two *n*-hexane molecules adsorbed on close non-interacting Brønsted OH groups in an Al-rich H-*BEA/5 model zeolite. View along the *b* (left) and *a* (right) dimensions. The Van der Waals dispersion forces between the *n*-hexane molecules increase the overall adsorption energy by 11 kJ.mol^{-1}.

Thus the increase in the adsorption energy due to mutual interactions of *n*-hexane molecules sited on close non-interacting strongly acidic sites of Al-rich H-*BEA zeolite could significantly decrease the apparent activation energy (for illustration see the energy diagram in Figure 7). The calculated increase in the adsorption energy due to possible mutual interaction between the *n*-hexane molecules is in a good agreement with the decrease in the apparent activation energy experimentally found for the Al-rich *BEA catalyst.

In contrast to superacids, where the reaction rate of *n*-hexane skeletal isomerization is predominantly controlled by the acid strength of acid sites located in unconfined space,[5] the dominant factors controlling the reaction over the Al-rich H-*BEA zeolite are given by guest−host and guest−guest van der Waals interactions. Recently, Jones et al.[21] examined the effects of the Al density on the reactivity of protons for dehydration of CH_3OH in the MFI zeolite to probe how the Al density influences the strength and location of Brønsted acid sites. In accordance with our results, they concluded that the acid strength is practically independent of the acid site concentration and the observed specific reactivity enhancement with increasing concentrations of protonic sites arises from increased van der Waals interactions in the confining voids and the corresponding adsorption energy. However, the 10-MR channel system of the ZSM-5 zeolite cannot provide sufficient space for the interaction of two linear molecules of C_6 hydrocarbons;[76] in addition, the density of the acid sites is limited due to the absence of a synthesis procedure for the preparation of zeolite with molar Si/Al ratio below ca 11. The unique arrangement and density of active sites in Al-rich H-*BEA zeolite in the three-dimensional channel system with 12-MR openings is not available in other zeolitic structures.

In summary, the achievement of the high concentration of non-interacting acidic protons in the zeolite catalyst allowed a dramatic increase in the isomerization activity and a shift of the operation temperature window into the thermodynamically more favourable region for desired di-branched isomers. The negative charge of the Al-Si-Al sequences facing different channels provides the unique concentration of protonic sites in the three-dimensional channel system with 12-MR openings providing easy transport of reactants and products. It is a significant advantage over traditional mordenite based isomerization catalysts where the pseudo-monodimensional channel structure and the restricted accessibility of acid sites located in 8-MR channels limit the efficiency of the catalytic process by mass transfer effects.[78] Al-rich H-*BEA is also advantageous to Y zeolites, wherein the protonic sites are mutually affected due to the presence of Al-Si-Al sequences in the framework and exhibit much lower acid strengths.[79] Conversely, there are no spectroscopic signatures of significantly different acidic characteristics in the Al-rich beta zeolite. Because the enhancement of the

strength of the acid groups has not been observed, the increase in specific activity of close non-interacting OH groups must be accompanied with another specific synergistic effect. We investigated the possible influence of adjacent active centers on the interaction of molecules of C_6 hydrocarbons on close non-interacting bridging OH groups. The theoretical calculations using approximations considering *n*-hexane molecules suggest that the interaction of molecules on nearby active centers can contribute to a higher adsorption energy and this increase is consistent with the decrease of the apparent activation energy. This is not an exhaustive rigorous proof that the synergistic effect is only based on the mutual interaction of C_6 molecules increasing the adsorption energy with the corresponding reduction of the apparent activation energy, but it may represent one of likely explanations. However, we can not rule out that the overall increase in specific activity is given by contributions from others synergistic effects. Effects of the proximity of Brønsted and Lewis sites,[80] the arrangement of acid centers influencing the entropy of the system[81,82] or an interaction of one molecule with two close centers could possibly affect the overall catalytic process and need to be accessed in further studies.

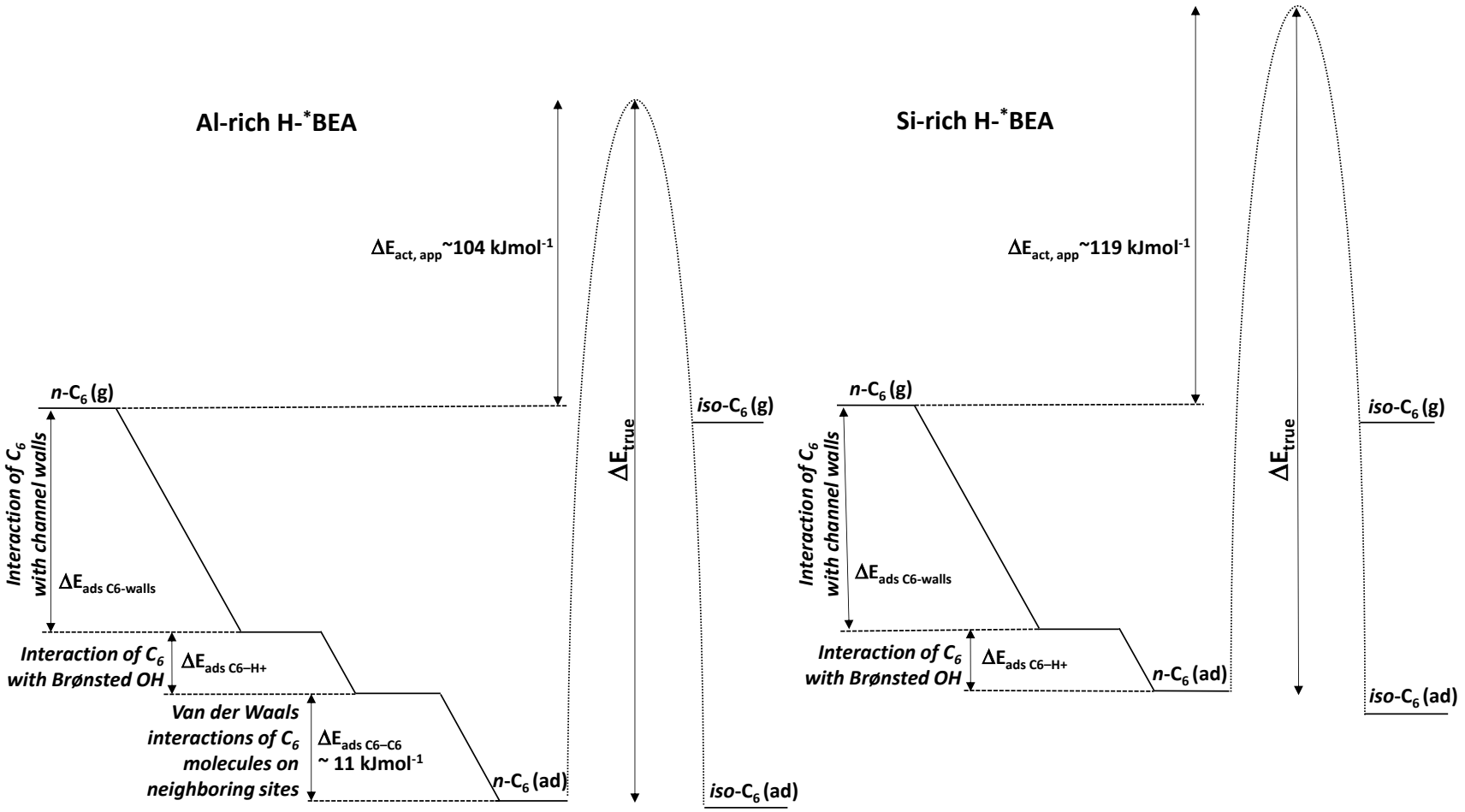

Figure 7. Simplified energy diagrams for acid-catalyzed reaction steps of isomerization of *n*-hexane over A) Al-rich and B) Si-rich H-*BEA zeolites. The true (intrinsic) activation energy ΔE_{true} of isomerization is given by the sum of the apparent activation energy $E_{act,\ app}$ and the adsorption energies ($\Delta E_{ads\ C6\text{-}walls} + \Delta E_{ads\ C6\text{-}H+} + \Delta E_{ads\ C6\text{-}C6}$). Van der Waals interactions of two co-adsorbed C_6 molecules on close Brønsted OH groups ($\Delta E_{ads\ C6\text{-}C6}$) increase the adsorption heat by ~ 11 kJmol^{-1} for Al-rich H-*BEA. The apparent activation energy of isomerization can be correspondingly lowered for Al-rich H-*BEA.

*3.5. Implication of the enhanced activity of Al-rich H-*BEA on isomerization of alkanes*

It is well established that mordenite zeolites with strongly acidic bridging Si-OH-Al sites are the most active and selective among all the types of investigated zeolitic hydroisomerization catalysts.[3,11,12,18,83,84] However, considerably lower activity of mordenite zeolites compared to chlorinated alumina necessitates isomerization at higher temperatures leading to unfavorable thermodynamic equilibrium for branched isomers. An essential solution of the problem lies in significant enhancement of the isomerization activity that enables reaching high conversions at lower temperatures in a favorable area of the thermodynamic equilibrium. The remarkable increase in the yield of branched isomers and an increase in the selectivity for the desired products limiting cracking reactions over Al-rich Pt/H-*BEA enables a shift of the operation window to lower temperatures. To analyze the potential of the Al-rich *BEA zeolite as an environmentally sustainable low/medium temperature hydroisomerization catalyst, the activity, selectivity and durability of Al-rich Pt/H-*BEA were compared with state-of-the-art microporous and micro-mesoporous mordenite zeolites under model reaction conditions and also the relevant conditions of the hydroisomerization process, i.e. at elevated pressure and at high concentrations of *n*-hexane in the reaction stream. The yields of branched hexane isomers and C_1-C_5 by-products as a function of temperature at low pressures of *n*-hexane compared for Al-rich Pt/H-*BEA/4.2 and microporous and micro-mesoporous Pt/H-mordenite zeolites are shown in figure 8. The distribution of the formed mono-branched isomers (2-methylpentane and 3-methylpentane) and di-branched isomers (2,2-dimethylbutane and 2,3-dimethyl butane) is listed in Table S1. The yield of branched isomers was approximately 7 times higher (at 175 °C) over Al-rich BEA than over MOR, while the yield of C_1-C_5 by-products was comparable or lower to that over mordenite catalysts. The performance of the mordenite catalysts was comparable to Si-rich *BEA catalysts.

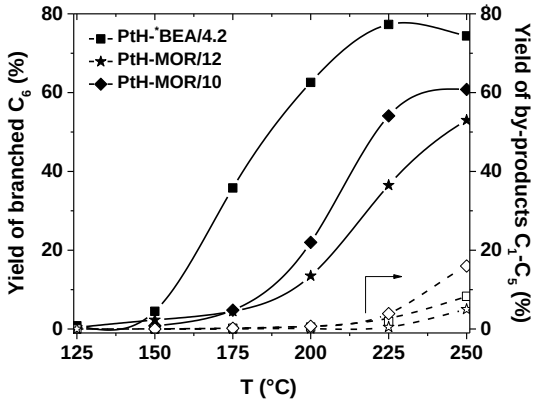

Figure 8. Comparison of Al-rich *BEA (PtH-*BEA/4.2) with microporous PtH-MOR/12 and partially dealuminated micro-mesoporous PtH-MOR/10 zeolites in hydroisomerization of *n*-hexane. Effect of temperature on the yields of branched C_6 isomers and C_1-C_5 by-products.

The performance characteristics of Al-rich Pt/H-*BEA compared to Si-rich Pt/H-*BEA and MOR zeolites under elevated pressure and at high concentration of hexane in the hydrogen stream relevant to the catalytic processes are listed in table 3. A threefold increase in the concentration of the active sites and the synergetic effect clearly resulted in the desired increase in activity and selectivity. The Al-rich Pt/H-*BEA/4.2 gives an isomer yield of 51.1% at a temperature of 200 °C, whereas the Si-rich Pt/H-zeolites lead to isomers yields from 10.1 to 12.1% at the same temperature. Stable values of the yields of isomers ~77% and by-products ~1.2% as a function of time-on-stream were obtained at 215 °C for 72 h that indicates stability of the Al-rich Pt/H-*BEA. It is clear that the unique density and distribution of the strongly acidic sites are ultimately connected with catalytic performance highly exceeding that of state-of-the-art Si-rich zeolite catalysts.

Table 3. The yields of branched hexane isomers and lower molecular weight by-products for hydroisomerization of *n*-hexane analyzed under process-like conditions.

	PtH-BEA/4.2		PtH-BEA/12		PtH-MOR/12		PtH-MOR/10	
	200 °C	215 °C	200 °C	215 °C	200 °C	215 °C	200 °C	215 °C
$y_{\Sigma iso\text{-}C6}$ (%)	51.1	76.8	12.1	31.8	10.1	25.4	10.5	28.1
$y_{2MP+3MP}$ (%)	44.8	62.1	11.9	29.1	8.8	21.8	9.5	24.5
$y_{2,2DMB}$ (%)	1.5	6.7	0.08	1.5	0.32	1	0.95	0.95
$y_{2,3DMB}$ (%)	4.8	8	0.2	1.2	0.93	2.6	0.86	2.67
$y_{by\text{-}products\ C1\text{-}C4}$ (%)	0.11	1.2	10.7	26.7	0.58	1.3	0.65	1.7

Reaction conditions: WHSV 0.7 h^{-1}, molar ratio H_2/n-C_6 6, pressure 10 bar.

[a] Calculated using the first-order kinetics.

[b] TOF calculated for total concentration of Al.

Conclusions

The critical function of the density of the acidic protons for hydroisomeroization of *n*-hexane was elucidated using the H-forms of the beta zeolites with a very high concentration of aluminum (Si/Al ≥ 4) with highly predominant tetrahedrally coordinated Al atoms in the framework. Analysis of the relationships between the density and distribution of strongly acidic sites and *n*-hexane isomerization identified a specific arrangement of Brønsted acid sites directing the reaction toward higher reaction rates. A high density of strongly acidic non-interacting close OH groups lowers the activation barrier in the isomerization reaction and results in multiplying the reaction rates by a factor of six compared to the hitherto most active Si-rich zeolite catalysts. The arrangement of Brønsted acid sites is unique for the Al-rich H-*BEA zeolite (Si/Al ~ 4) and is given by the arrangement of Al atoms in the Al-Si-Al sequences charge-balanced by two H^+ ions located in different zeolite channels. Understanding the consequences of the arrangement of Brønsted acid sites in the channels of Al-rich H-*BEA zeolite opens a new pathway for both elucidation of fundamental aspects of governing of the active sites in acid-catalyzed reactions as well as for tailoring the properties of zeolite-based catalysts for to obtain enhanced functionality.

Supporting Information

X-ray diffraction patterns (Figure S1) and the distribution of products for hydroisomerization of *n*-hexane for the studied catalysts (Table S1) are provided in the Supporting Information.

Acknowledgments

This work was supported by the Czech Science Foundation under project # 15-12113S and RVO: 61388955. This work was supported by the IT4Innovations Centre of Excellence project (CZ.1.05/1.1.00/02.0070), funded by the European Regional Development Fund and the national budget of the Czech Republic via the Research and Development for Innovations Operational Programme, as well as by the Czech Ministry of Education, Youth and Sports via the Large Research, Development and Innovations Infrastructures project (LM2011033). The authors acknowledge the assistance provided by the Research Infrastructure NanoEnviCz, supported by the Ministry of Education, Youth and Sports of the Czech Republic under Project No. LM2015073.

References

(1) Iglesia, E.; Soled, S. L.; Kramer, G. M. *J. Catal.* **1993**, *144*, 238-253.

(2) Iglesia, E.; Barton, D. G.; Soled, S. L.; Miseo, S.; Baumgartner, J. E.; Gates, W. E.; Fuentes, G. A.; Meitzner, G. D. In *Stud. Surf. Sci. Catal.* 1996; Vol. 101 A, p 533.

(3) Chica, A.; Corma, A. *J. Catal.* **1999**, *187*, 167-176.

(4) Ono, Y. *Catal. Today* **2003**, *81*, 3-16.

(5) Knaeble, W.; Carr, R. T.; Iglesia, E. *J. Catal.* **2014**, *319*, 283-296.

(6) Digne, M.; Raybaud, P.; Sautet, P.; Guillaume, D.; Toulhoat, H. *J. Am. Chem. Soc.* **2008**, *130*, 11030-11039.

(7) Gora, L.; Jansen, J. C. *J. Catal.* **2005**, *230*, 269-281.

(8) Weyda, H.; Köhler, E. *Catal. Today* **2003**, *81*, 51-55.

(9) Shakun, A. N.; Fedorova, M. L. *Catal. Ind.* **2014**, *6*, 298-306.

(10) Sazama, P.; Sobalik, Z.; Dedecek, J.; Jakubec, I.; Parvulescu, V.; Bastl, Z.; Rathousky, J.; Jirglova, H. *Angew. Chem. Int. Ed.* **2013**, *52*, 2038-2041.

(11) Tromp, M.; van Bokhoven, J. A.; Oostenbrink, M. T. G.; Bitter, J. H.; de Jong, K. P.; Koningsberger, D. C. *J. Catal.* **2000**, *190*, 209-214.

(12) Konnov, S. V.; Ivanova, I. I.; Ponomareva, O. A.; Zaikovskii, V. I. *Microporous Mesoporous Mater.* **2012**, *164*, 222-231.

(13) Barton, D. G.; Soled, S. L.; Meitzner, G. D.; Fuentes, G. A.; Iglesia, E. *J. Catal.* **1999**, *181*, 57-72.

(14) Yadav, G. D.; Nair, J. J. *Microporous Mesoporous Mater.* **1999**, *33*, 1-48.

(15) Olah, G. A.; Mo, Y. K.; Olah, J. A. *J. Am. Chem. Soc.* **1973**, *95*, 4939-4951.

(16) Kramer, G. J.; Vansanten, R. A.; Emeis, C. A.; Nowak, A. K. *Nature* **1993**, *363*, 529-531.

(17) Corma, A.; Orchillés, A. V. *Microporous Mesoporous Mater.* **2000**, *35–36*, 21-30.

(18) Chiang, H.; Bhan, A. *J. Catal.* **2011**, *283*, 98-107.

(19) Haag, W. O.; Lago, R. M.; Weisz, P. B. *Nature* **1984**, *309*, 589-591.

(20) Janda, A.; Bell, A. T. *J. Am. Chem. Soc.* **2013**, *135*, 19193-19207.

(21) Jones, A. J.; Carr, R. T.; Zones, S. I.; Iglesia, E. *J. Catal.* **2014**, *312*, 58-68.

(22) Sazama, P.; Dedecek, J.; Gabova, V.; Wichterlova, B.; Spoto, G.; Bordiga, S. *J. Catal.* **2008**, *254*, 180-189.

(23) Xie, B.; Song, J.; Ren, L.; Ji, Y.; Li, J.; Xiao, F. S. *Chem. Mater.* **2008**, *20*, 4533-4535.

(24) Shanjiao, K.; Tao, D.; Qiang, L.; Aijun, D.; Yanying, Z.; Huifang, P. *J. Porous Mater.* **2008**, *15*, 159-162.

(25) Majano, G.; Delmotte, L.; Valtchev, V.; Mintova, S. *Chem. Mater.* **2009**, *21*, 4184-4191.

(26) Kamimura, Y.; Chaikittisilp, W.; Itabashi, K.; Shimojima, A.; Okubo, T. *Chem. - Asian J.* **2010**, *5*, 2182-2191.

(27) Kamimura, Y.; Tanahashi, S.; Itabashi, K.; Sugawara, A.; Wakihara, T.; Shimojima, A.; Okubo, T. *J. Phys. Chem. C* **2011**, *115*, 744-750.

(28) Xie, B.; Zhang, H.; Yang, C.; Liu, S.; Ren, L.; Zhang, L.; Meng, X.; Yilmaz, B.; Muller, U.; Xiao, F.-S. *Chem. Commun. (Cambridge, U. K.)* **2011**, *47*, 3945-3947.

(29) Itabashi, K.; Kamimura, Y.; Iyoki, K.; Shimojima, A.; Okubo, T. *J. Am. Chem. Soc.* **2012**, *134*, 11542-11549.

(30) Yilmaz, B.; Muller, U.; Feyen, M.; Maurer, S.; Zhang, H.; Meng, X.; Xiao, F. S.; Bao, X.; Zhang, W.; Imai, H.; Yokoi, T.; Tatsumi, T.; Gies, H.; De Baerdemaeker, T.; De Vos, D. *Catal. Sci. Technol.* **2013**, *3*, 2580-2586.

(31) De Baerdemaeker, T.; Yilmaz, B.; Muller, U.; Feyen, M.; Xiao, F. S.; Zhang, W.; Tatsumi, T.; Gies, H.; Bao, X.; De Vos, D. *J. Catal.* **2013**, *308*, 73-81.

(32) Zhang, H.; Xie, B.; Meng, X.; Mueller, U.; Yilmaz, B.; Feyen, M.; Maurer, S.; Gies, H.; Tatsumi, T.; Bao, X.; Zhang, W.; De Vos, D.; Xiao, F.-S. *Microporous Mesoporous Mater.* **2013**, *180*, 123-129.

(33) Kubota, Y.; Itabashi, K.; Inagaki, S.; Nishita, Y.; Komatsu, R.; Tsuboi, Y.; Shinoda, S.; Okubo, T. *Chem. Mater.* **2014**, *26*, 1250-1259.

(34) Zheng, B.; Wan, Y.; Yang, W.; Ling, F.; Xie, H.; Fang, X.; Guo, H. *Chin. J. Catal.* **2014**, *35*, 1800-1810.

(35) Sazama, P.; Wichterlova, B.; Sklenak, S.; Parvulescu, V. I.; Candu, N.; Sadovska, G.; Dedecek, J.; Klein, P.; Pashkova, V.; Stastny, P. *J. Catal.* **2014**, *318*, 22-33.

(36) Borade, R. B.; Clearfield, A. *Microporous Mater.* **1996**, *5*, 289-297.

(37) Borade, R. B.; Clearfield, A. *Chem. Commun. (Cambridge, U. K.)* **1996**, 625-626.

(38) Wichterlova, B.; Tvaruzkova, Z.; Sobalik, Z.; Sarv, P. *Microporous Mesoporous Mater.* **1998**, *24*, 223-233.

(39) Fyfe, C. A.; Feng, Y.; Grondey, H.; Kokotailo, G. T.; Gies, H. *Chem. Rev. (Washington, DC, U. S.)* **1991**, *91*, 1525-1543.

(40) Engelhardt, G.; Lohse, U.; Lippmaa, E.; Tarmak, M.; Magi, M. *Z. Anorg. Allg. Chem.* **1981**, *482*, 49-64.

(41) Van De Runstraat, A.; Kamp, J. A.; Stobbelaar, P. J.; Van Grondelle, J.; Krijnen, S.; Van Santen, R. A. *J. Catal.* **1997**, *171*, 77-84.

(42) Kresse, G.; Hafner, J. *Phys. Rev. B* **1993**, *48*, 13115-13118.

(43) Kresse, G.; Hafner, J. *Phys. Rev. B* **1994**, *49*, 14251-14269.

(44) Kresse, G.; Furthmuller, J. *Phys. Rev. B* **1996**, *54*, 11169-11186.

(45) Kresse, G.; Furthmuller, J. *Comput. Mater. Sci.* **1996**, *6*, 15-50.

(46) Blochl, P. E. *Phys. Rev. B* **1994**, *50*, 17953-17979.

(47) Kresse, G.; Joubert, D. *Phys. Rev. B* **1999**, *59*, 1758-1775.

(48) Perdew, J. P.; Burke, K.; Ernzerhof, M. *Phys. Rev. Lett.* **1996**, *77*, 3865-3868.

(49) Tkatchenko, A.; Scheffler, M. *Phys. Rev. Lett.* **2009**, *102*, 073005.

(50) Bucko, T.; Lebegue, S.; Hafner, J.; Angyan, J. G. *Phys. Rev. B* **2013**, *87*, *064110*.

(51) Grimme, S. *J. Comput. Chem.* **2006**, *27*, 1787-1799.

(52) Muller, M.; Harvey, G.; Prins, R. *Microporous Mesoporous Mater.* **2000**, *34*, 135-147.

(53) Huo, H.; Peng, L.; Gan, Z.; Grey, C. P. *J. Am. Chem. Soc.* **2012**, *134*, 9708-9720.

(54) Strodel, P.; Neyman, K. M.; Knozinger, H.; Rosch, N. *Chem. Phys. Lett.* **1995**, *240*, 547-552.

(55) Sigl, M.; Ernst, S.; Weitkamp, J.; Knozinger, H. *Catal. Lett.* **1997**, *45*, 27-33.

(56) Kiricsi, I.; Flego, C.; Pazzuconi, G.; Parker, W. O.; Millini, R.; Perego, C.; Bellussi, G. *J. Phys. Chem.* **1994**, *98*, 4627-4634.

(57) Brus, J.; Kobera, L.; Schoefberger, W.; Urbanová, M.; Klein, P.; Sazama, P.; Tabor, E.; Sklenak, S.; Fishchuk, A. V.; Dědeček, J. *Angew. Chem. Int. Ed.* **2015**, *54*, 541-545.

(58) Sazama, P.; Wichterlova, B.; Dedecek, J.; Tvaruzkova, Z.; Musilova, Z.; Palumbo, L.; Sklenak, S.; Gonsiorova, O. *Microporous Mesoporous Mater.* **2011**, *143*, 87-96.

(59) Bourgeat-Lami, E.; Massiani, P.; Di Renzo, F.; Espiau, P.; Fajula, F.; Des Courieres, T. *Appl. Catal.* **1991**, *72*, 139-152.

(60) Beck, L. W.; Haw, J. F. *J. Phys. Chem.* **1995**, *99*, 1076-1079.

(61) De Menorval, L. C.; Buckermann, W.; Figueras, F.; Fajula, F. *J. Phys. Chem.* **1996**, *100*, 465-467.

(62) Kunkeler, P. J.; Zuurdeeg, B. J.; Van Der Waal, J. C.; Van Bokhoven, J. A.; Koningsberger, D. C.; Van Bekkum, H. *J. Catal.* **1998**, *180*, 234-244.

(63) Kuehl, G. H.; Timken, H. K. C. *Microporous Mesoporous Mater.* **2000**, *35-36*, 521-532.

(64) Penzien, J.; Abraham, A.; Van Bokhoven, J. A.; Jentys, A.; Muller, T. E.; Sievers, C.; Lercher, J. A. *J. Phys. Chem. B* **2004**, *108*, 4116-4126.

(65) Sazama, P.; Tabor, E.; Klein, P.; Wichterlova, B.; Sklenak, S.; Mokrzycki, L.; Pashkkova, V.; Ogura, M.; Dedecek, J. *J. Catal.* **2016**, *333*, 102-114.

(66) Anderson, J. R.; Chang, Y. F.; Western, R. J. *J. Catal.* **1989**, *118*, 466-482.

(67) Bjørgen, M.; Bonino, F.; Kolboe, S.; Lillerud, K. P.; Zecchina, A.; Bordiga, S. *J. Am. Chem. Soc.* **2003**, *125*, 15863-1568.

(68) Ma, M.; Johnson, K. E. *J. Am. Chem. Soc.* **1995**, *117*, 1508-1513.

(69) Hemelsoet, K.; Qian, Q.; De Meyer, T.; De Wispelaere, K.; De Sterck, B.; Weckhuysen, B. M.; Waroquier, M.; Van Speybroeck, V. *Chem. Eur. J.* **2013**, *19*, 16595-16606.

(70) Sazama, P.; Mokrzycki, L.; Wichterlova, B.; Vondrova, A.; Pilar, R.; Dedecek, J.; Sklenak, S.; Tabor, E. *J. Catal.* **2015**, *332*, 201-211.

(71) Narbeshuber, T. F.; Vinek, H.; Lercher, J. A. *J. Catal.* **1995**, *157*, 388-395.

(72) Wei, J. *Chem. Eng. Sci.* **1996**, *51*, 2995-2999.

(73) Katada, N.; Suzuki, K.; Noda, T.; Miyatani, W.; Taniguchi, F.; Niwa, M. *Appl. Catal., A* **2010**, *373*, 208-213.

(74) Haag, W. O. In *Stud. Surf. Sci. Catal* 1994; Vol. 84, p 1375.

(75) Kotrel, S.; Knözinger, H.; Gates, B. C. *Microporous Mesoporous Mater.* **2000**, *35-36*, 11-20.

(76) Eder, F.; Lercher, J. A. *Zeolites* **1997**, *18*, 75-81.

(77) Yoda, E.; Kondo, J. N.; Domen, K. *J. Phys. Chem. B* **2005**, *109*, 1464.

(78) Tromp, M.; van Bokhoven, J. A.; Garriga Oostenbrink, M. T.; Bitter, J. H.; de Jong, K. P.; Koningsberger, D. C. *J. Catal.* **2000**, *190*, 209.

(79) Wang, N.; Zhang, M.; Yu, Y. *Microporous Mesoporous Mater.* **2013**, *169*, 47.

(80) Van Bokhoven, J. A.; Williams, B. A.; Ji, W.; Koningsberger, D. C.; Kung, H. H.; Miller, J. T. *J. Catal.* **2004**, *224*, 50-59.

(81) Bhan, A.; Gounder, R.; Macht, J.; Iglesia, E. *J. Catal.* **2008**, *253*, 221-224.

(82) Janda, A.; Vlaisavljevich, B.; Lin, L.-C.; Mallikarjun Sharada, S.; Smit, B.; Head-Gordon, M.; Bell, A. T. *J. Phys. Chem. C* **2015**, *119*, 10427-10438.
(83) Chao, K. J.; Wu, H. C.; Leu, L. J. *Appl. Catal., A* **1996**, *143*, 223-243.
(84) Viswanadham, N.; Dixit, L.; Gupta, J. K.; Garg, M. O. *J. Mol. Catal. A Chem.* **2006**, *258*, 15-21.